PAN

Opto-Electronics Review

journal homepage: https://journals.pan.pl/opelre

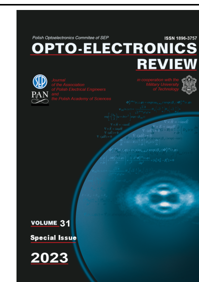

InAs/InAsSb superlattice infrared detectors

David Z. Ting*, Alexander Soibel, Arezou Khoshakhlagh, Sam A. Keo, Sir B. Rafol, Anita M. Fisher, Cory J. Hill, Brian J. Pepper, Yuki Maruyama, Sarath D. Gunapala

NASA Jet Propulsion Laboratory, California Institute of Technology, 4800 Oak Grove Dr., Pasadena, CA 91109-8099, USA

Article info

Article history:
Received 19 Oct. 2022
Received in revised form 15 Dec. 2022
Accepted 21 Dec 2022
Available on-line 24 Feb. 2023

Keywords:
Infrared detector; type-II superlattice; InAs/InAsSb; complementary barrier infrared detectors; strained layer superlattice.

Abstract

Mid-wavelength infrared detectors and focal plane array based on n-type InAs/InAsSb type-II strained layer superlattice absorbers have achieved excellent performance. In the long and very long wavelength infrared, however, n-type InAs/InAsSb type-II strained layer superlattice detectors are limited by their relatively small absorption coefficients and short growth-direction hole diffusion lengths, and consequently have only been able to achieve modest level of quantum efficiency. The authors present an overview of their progress in exploring complementary barrier infrared detectors that contain p-type InAs/InAsSb type-II strained layer superlattice absorbers for quantum efficiency enhancement. The authors describe some representative results, and also provide additional references for more in-depth discussions. Results on InAs/InAsSb type-II strained layer superlattice focal plane arrays for potential NASA applications are also briefly discussed.

1. Introduction

The development of InAs/InAsSb/InSb type-II strained layer superlattice (T2SLS) for infrared emitter and detector applications actually predates that of the more established InAs/Ga(In)Sb T2SLS [1]. The original motivation was to take advantage of the type-II band alignment and strain-induced band-gap reduction to achieve cut-off wavelengths longer than possible with bulk InAsSb alloy [2]. InAsSb/InSb T2SLS grown on InSb substrates [3] and InAs/InAsSb T2SLS grown on GaAs [4] and InAs [5] substrates were demonstrated in the 1990s. It was found that InAs/InAsSb strained layer superlattice (SLS) with band gap comparable to InSb demonstrated substantially suppressed Auger processes when compared to InSb, and that the Shockley-Read contributions to recombination rates were low [6]. In the decade following the year 2000, research activities in InAs/GaSb type-II superlattices (T2SL) accelerated while the development in InAsSb SLS became dormant. The re-emergence came in 2009 with the report of strain-balanced growth of InAs/InAsSb SLS structures on GaSb, exhibiting photoluminescence (PL) emissions in the 5–10 µm range [7]. The 2011 finding of significantly longer minority carrier lifetimes in InAs/InAsSb T2SLS [8] than in InAs/GaSb T2SL [9] (both ~8 µm) generated much renewed interest in this material; results in mid-wavelength infrared (MWIR) and longer long-wavelength infrared (LWIR) also demonstrated longer lifetimes in InAs/InAsSb T2SLS than in InAs/GaSb T2SL [10–13]. This was soon followed by the demonstration of InAs/InAsSb SLS LWIR nBn detector in 2012 [14]. More discussions on the early development can be found in Refs. 15 and 16.

There has been a considerable development in InAs/InAsSb T2SLS detectors in recent years. The versatility of the InAs/InAsSb T2SLS has resulted in the demonstration of MWIR [17], LWIR [14, 18], very long wavelength infrared (VLWIR) [19], and bias-selectable MWIR/LWIR dual-band infrared photodetectors [20]. While most of the more recent InAs/InAsSb T2SLS have been grown on (100) GaSb substrates, growths by a variety of modes have also been demonstrated. Growths on GaAs [21], Si [22, 23], Ge-Si [24], and AlSb (via metamorphic buffer on GaSb) [25] have been reported. Growths of MWIR and LWIR detectors on (211)A and B, and (311)A and B GaSb substrates have also been reported [26, 27].

The development of InAs/InAsSb superlattice infrared detectors at the NASA Jet Propulsion Laboratory (JPL) was originally motivated by the desire to extend the cut-off wavelength of the bulk nBn detectors [28] from ~3.2 µm (for InAs absorber) and ~4.1 µm (for InAsSb absorber) to

*Corresponding author at: david.z.ting@jpl.nasa.gov

https://doi.org/10.24425/opelre.2023.144565
1896-3757/ Association of Polish Electrical Engineers (SEP) and Polish Academic of Sciences (PAS). Published by PAS.
Government sponsorship acknowledged.
© 2023 California Institute of Technology. This is an open access article under the CC BY license (http://creativecommons.org/licenses/by/4.0/).

match that of InSb (~5.3 µm) in order to cover the entire 3 to 5 µm MWIR atmospheric transmission window. Beginning in 2008, the authors experimented with various absorbers, including InSb quantum dots embedded in InAsSb matrix, InSb/InAsSb SLS, and InSb/InAs SLS, and eventually succeeded in 2010 with the InAs/InAsSb SLS. Details of this development are described in Ref. 29. The initial detector and focal plane array (FPA) results were first disclosed in a patent publication 30, with more details reported in subsequent publications 31, 32. Significantly, MWIR InAs/InAsSb SLS FPAs have demonstrated a 40–50 K operating temperature advantage over InSb FPAs [31, 32], while retaining the same III–V semiconductor benefits of uniformity, high operability, and manufacturability. This has established the InAs/InAsSb T2SLS as an important infrared detector material. Although the InAs/InAsSb T2SLS nBn detector has led to excellent MWIR FPA performance, there are challenges in the extension to the LWIR and the VLWIR. The remainder of the paper provides a brief overview of VLWIR InAs/InAsSb T2SLS detector development at JPL and provides additional references to more detailed discussions in the authors' published work.

2. InAs/InAsSb superlattice detector development

2.1. *LWIR challenges*

One of the challenges for the VLWIR InAs/InAsSb T2SLS is that its absorption coefficient is smaller than that of the InAs/GaSb T2SL [33, 34], and would then require a thicker absorber layer to achieve comparable quantum efficiency (QE). Also, to achieve longer cut-off wavelength requires the use of superlattice with longer period, which in turn leads to smaller electron–hole wavefunction overlap and weaker absorption coefficient. Here again, thicker absorber would be needed for longer cut-off T2SLS in order to maintain the desired QE level. But at the same time, the growth-direction hole conductivity effective mass of VLWIR InAs/InAsSb T2SLS can be quite large [35, 36], leading to low hole mobility and short hole diffusion length along the growth direction. Short hole diffusion length limits the viable thickness of n-type InAs/InAsSb T2SLS absorber. Therefore, in general, the attainable QE for VLWIR InAs/InAsSb T2SLS nBn or XBn [37] detectors is limited. Moreover, the achievable QE also becomes progressively smaller as the detector cut-off wavelength increases. To briefly illustrate this, in Fig. 1, the authors show the spectral QE for a set of unipolar barrier detectors samples with n-type InAs/InAsSb T2SLS absorbers; the absorber thicknesses range from 1.9 to 3.8 µm. While all the detectors have good dark current characteristics, their QE shows a general decreasing trend as the cut-off wavelength increases. While there can be exceptions (due to, for instance, material quality variations), the general trend is valid. Additional discussions on the VLWIR InAs/InAsSb T2SLS challenges can be found in Ref. 38.

2.2. *Detector architecture*

The VLWIR QE problem can be addressed by using p-type T2SLS absorbers, which provide higher mobility and longer diffusion lengths for minority carriers (electrons).

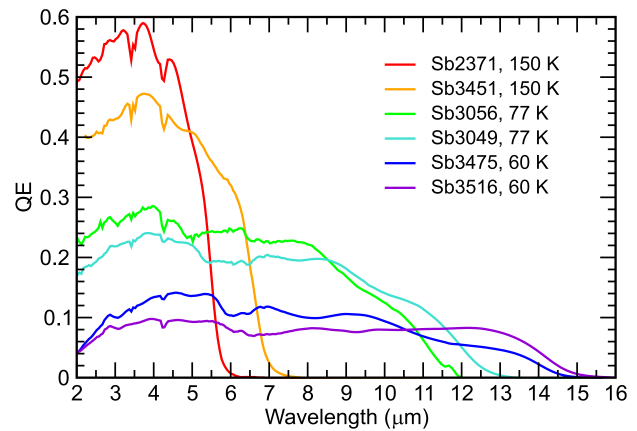

Fig. 1. Spectral QE for detectors with n-type InAs/InAsSb superlattice absorbers of different cut-off wavelengths. Detectors are not anti-reflection coated.

A suitable device architecture for p-type absorber is the complementary barrier infrared detector (CBIRD). The CBIRD has a non-equilibrium device architecture [39–41], where, under reverse bias, the minority density is reduced to below equilibrium values through exclusion and extraction [42]. The CBIRD structure consists of an infrared absorber surrounded by a unipolar electron barrier on one side, and a hole unipolar barrier on the other side, and is capped by top and bottom contact layers at the two ends. The CBIRD was originally implemented for the p-type InAs/GaSb T2SL absorber, using a shorter-period InAs/GaSb T2SL as the electron barrier, and an InAs/AlSb superlattice as the hole barrier [43, 44]. CBIRD with InAs/InAsSb T2SLS absorber can be realised using a shorter-period (larger band gap) InAs/InAsSb T2SLS as the unipolar hole barrier (this is feasible since the conduction bands of different InAs/InAsSb superlattices are approximately aligned, leaving their band offsets mostly in the valence band), and a bulk AlGaAsSb alloy layer as the unipolar electron barrier. It can be noted that AlGaAsSb is already used as the unipolar electron barrier for the MWIR InAs/InAsSb T2SLS nBn [31, 32].

The CBIRD is a flexible architecture that can accommodate both the n-type absorber (n-CBIRD) and the p-type absorber (p-CBIRD). The n-CBIRD may be thought of as an nBn/XBn with an added wide-gap emitter contact for reducing minority carrier injection (exclusion). Therefore, the VLWIR n-CBIRD benefits from generation-recombination (G-R) and surface leakage dark current suppression in the same manner as the nBn/XBn. But as discussed earlier, the maximum attainable QE with n-type T2SLS absorbers is limited. Absorber band gap grading, introduced by gradually varying the absorber superlattice period, can be used to create a built-in quasi-electric field to facilitate hole transport through drift in the n-type absorber; this can provide some QE enhancement.

Figure 2(a) shows the schematic structure for a p-CBIRD. For pixel delineation and isolation in a p-CBIRD detector array, it is needed to etch through the p-type absorber and past the p-n junction. This exposes the sidewalls of the p-type InAs/InAsSb T2SLS absorber, as illustrated in Fig. 2(a). The exposed surface of the p-type InAs/InAsSb T2SLS inverts to degenerate n-type, which can lead to two potential issues. First, the n^+ surface provides an electron conduction path that can lead to

electron surface leakage dark current (sidewall shunt current). But as shown in Fig. 2(a), in the CBIRD structure, the electron surface leakage path is interrupted by the electron unipolar barrier [45, 46], and, thus, the shunt current is blocked. The second issue is that the degenerate n-type surface also creates a surface p-n junction with a sub-surface depletion region and is subject to various surface dark current mechanisms [45, 47]. Good surface passivation for the p-type InAs/InAsSb T2SLS absorber is therefore highly desirable.

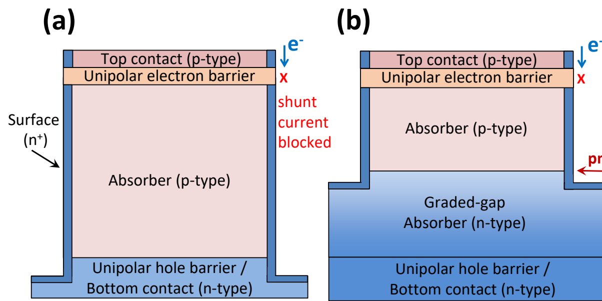

Fig. 2. Schematic illustration of pixel structures of two CBIRD structures: a p-CBIRD, with p-type absorber (a), and a pn-CBIRD, with both p-type and n-type absorber sections (b).

The area of the exposed p-type T2SLS absorber surface can be reduced by using the pn-CBIRD structure [48–50]. Figure 2 shows that, in contrast to the p-CBIRD, in the pn-CBIRD a portion of the p-type absorber is replaced by an n-type absorber. With the same total absorber thickness, the pn-CBIRD can achieve the same QE as the p-CBIRD, provided that the thickness of the n-type absorber (which can be graded or non-graded) does not exceed the growth-direction hole diffusion length. In the pn-CBIRD, it is only needed to etch past the absorber p-n junction for detector array pixel delineation. The shallower mesa etch in the pn-CBIRD reduces fabrication demands and also decreases the exposed surface area of the p-type absorber. A drawback of the pn-CBIRD compared to the p-CBIRD is that it contains a p-n homojunction (recall that the nBn reduces G-R dark current by avoiding this). The pn-CBIRD still has exposed p-type absorber surface, and, like the p-CBIRD, would benefit from good surface passivation. Both the p-CBIRD and the pn-CBIRD can achieve higher VLWIR QE than the n-CBIRD, but at the expense of having worse dark current characteristics. It can be noted that deep etch in pn-CBIRD FPA may be desirable from crosstalk and modulation transfer function (MTF) considerations. In that case, an accumulated surface potential repels the minority carriers (holes) from the etched n-type InAs/InAsSb T2SLS absorber surface, which is consequently relatively benign. More discussions on the trade-offs among the n-CBIRD, the p-CBIRD, and the pn-CBIRD can be found in Refs. 49 and 50.

3. Detector results

The authors examine device results from a set of three consecutively grown VLWIR InAs/InAsSb T2SLS CBIRD samples with the same absorber thickness but different combinations of p-type and n-type absorbers. The samples were grown on three-inch-diameter Te-doped GaSb (100) substrates in a Veeco Applied-Epi Gen III molecular beam epitaxy chamber equipped with valved cracking sources for the Group V Sb2 and As2 fluxes. Sb3019 is a pn-CBIRD with a 2.5 µm thick p-type absorber and a 2.5 µm thick graded-gap n-type absorber. Sb3020 is also a pn-CBIRD, but with a 4 µm thick p-type absorber, and a 1 µm thick graded-gap n-type absorber. Sb3021 is a p-CBIRD with a 5 µm thick p-type absorber only. The detailed device structures of Sb3019 and Sb3021 are described in Ref. 49; Sb3020 is similar to Sb3019 except for the absorber combination.

Square mesa photodiodes with Ti/Pt/Au contacts were fabricated using standard optical lithography for responsivity and dark current measurements. Figure 3 shows the measured dark *J-V* characteristics of Sb3020 at temperatures ranging from 30 K to 148 K. The detector mesa size is 240×240 µm^2. Since the narrow-gap absorber of Sb3020 contains metallurgical (grown), as well as sidewall surface p-n junctions, Sb3020 is subject to tunnelling and G-R dark currents, which are very apparent in the *J-V* characteristics and in the inset Arrhenius analysis plot. The −0.15 V dark current density for Sb3020 at 60 K is 1.19·10^{-5} A/cm^2, which is a factor of ~26 higher than given by Rule 07 [51].

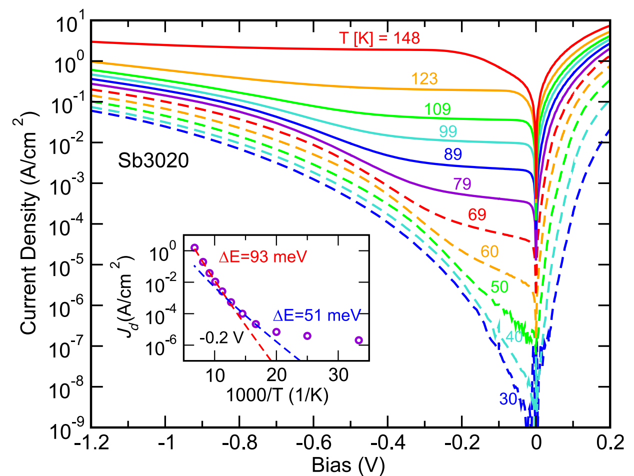

Fig. 3. Dark current density (J_d) as a function of applied bias, measured at temperatures ranging from 30 K to 148 K for a pn-CBIRD detector fabricated from Sb3020. The inset shows J_d temperature dependence at −0.2 V bias, with activation energies Δ*E* from Arrhenius analysis.

The Arrhenius plot in the inset of Fig. 3 shows the temperature dependence of dark current density under −0.2 V bias. For Sb3020 (nominal a band gap of 0.105 eV), the 89 K to 123 K activation energy of 0.093 eV indicates a mixture of diffusion and G-R dark current components; the 60 K to 79 K activation energy of 0.051 eV indicates G-R and tunnelling dark currents; and at 50 K and below tunnelling dark current appears to dominate. The dark current characteristics for Sb3019 and Sb3021 have been reported previously in Ref. 49; they are very similar to those for Sb3020 shown here.

Figure 4 shows the spectral QE derived from back-side illuminated spectral responsivity measured from 30 K to 80 K for the three CBIRD samples under −0.3 V bias. For Sb3019, Sb3020, and Sb3021, the turn-on biases are, respectively, −0.3, −0.15, and −0.1 V at 30 K, and −0.05, 0, and 0 V at 80 K. The spectral QE for Sb3019 and Sb3021 had been presented previously in Ref. 49; they are included

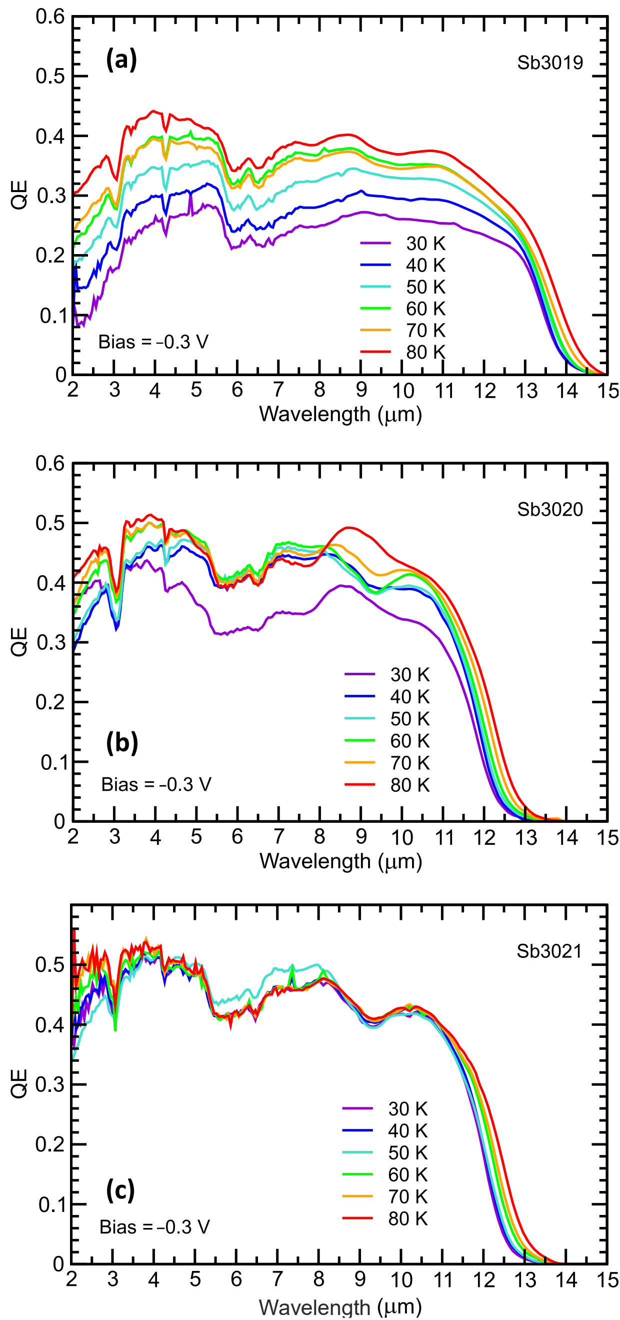

Fig. 4. Back-side illuminated spectral QE measured under −0.3 V bias at several temperatures for non-anti-reflection coated detectors fabricated from samples Sb3019 (a), Sb3020 (b), and Sb3021 (c).

here for comparison with the temperature dependence of the Sb3020 spectral QE. It can be seen very readily that all three samples have noticeably higher QE than n-type T2SLS absorber-based detectors of comparable cut-off wavelengths shown in Fig 1. From the 60 K device characteristics listed in Table 1, which includes cut-off wavelength, turn-on bias, QE (at 8.6 μm), and dark current density, it can be seen that all three samples can operate well at 60 K. However, it is also useful to examine the spectral QE at lower temperature in order to gain some insight into the differences between the p-CBIRD and the pn-CBIRD. For Sb3019, a systematic decrease in QE can be observed as the temperature is lowered from 80 to 30 K. For Sb3020, the QE decreases noticeably only at below 40 K. For Sb3021, there is no noticeable QE decrease all the way down to 30 K. Recall that while each of the three samples has the same total absorber thickness (5 μm), Sb3019 contains a 2.5 μm thick section of n-type absorber, Sb3020 a 1 μm thick section, and Sb3021 none. It is evident that the QE decrease is associated with reduction of hole diffusion length in the n-type absorber to below 2.5 μm as the temperature is lowered from 80 to 30 K. The fact that there is no QE decrease for Sb3021 indicates that the electron diffusion length in the p-type absorber in this temperature range is at least 5 μm.

Table 1.
Detector characteristics at 60 K.

Sample	$\lambda_{\text{Cut-off}}$ (μm)	Turn-on Bias (V)	QE @ 8.6 μm (%)	J_d (A/cm^2)
Sb3019	13.3	−0.15	33.4	$6.6 \cdot 10^{-5}$
Sb3020	11.8	−0.05	42.2	$1.2 \cdot 10^{-5}$
Sb3021	12.1	0	45.1	$3.0 \cdot 10^{-5}$

QE and dark current density are shown for −0.15 V bias.

Figure 5 compares the photocurrent and dark current temperature dependence for Sb3020. The photocurrent is determined from the integrated photo-response in the 8 to 12 μm spectral range for 300 K background and f/2 field of view (FOV) conditions. Taking the background limited infrared photodetection (BLIP) condition to be where the dark current is equal to the photocurrent, the estimated BLIP temperature is 87 K. For the more stringent BLIP condition of dark current being at ¼ of photocurrent, the corresponding BLIP temperature is 77 K.

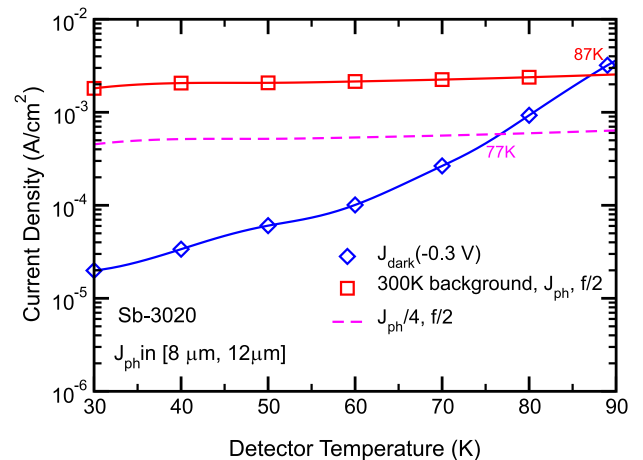

Fig. 5. Temperature dependence of photocurrent and dark current densities for Sb3020.

The authors have also calculated the specific detectivity from the spectral response, using an expression that includes dark current shot noise, photocurrent shot noise, and Johnson noise: $D^* = R_i\left[2q\left(J_\text{d} + J_\text{ph}\right) + 4k_\text{B}T/(RA)\right]^{-1/2}$, where R_i is the spectral responsivity, J_d and J_ph are respectively the dark and photocurrent densities, R is the detector dynamic resistance, and A is the mesa area. Figure 6 shows the calculated spectral D^* for the three samples as a function of wavelength; the D^* calculation includes the shot noise from the photocurrent in the spectral range shown in Fig 6 for 300 K background with f/2

condition. The inset shows the detector temperature dependence of black-body D^*, which includes the signal and noise from the integrated photocurrent in the 8–12 µm range. For comparison, the ideal black-body D^* (100% QE, zero dark current) is also shown. In the 30–70 K range, the calculated black-body D^* is within approximately a factor of two of the ideal value for each of the three samples.

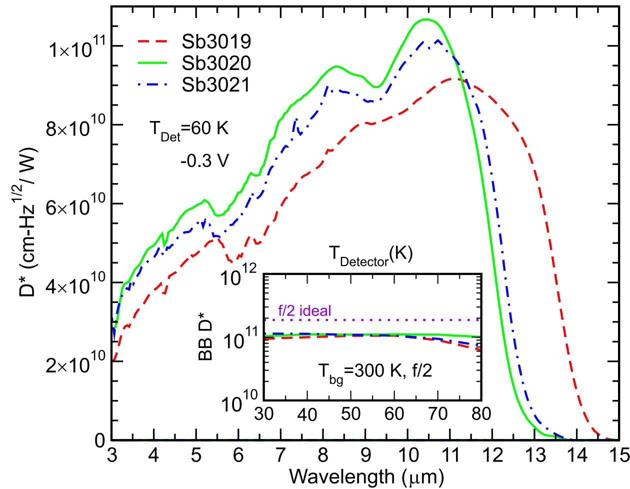

Fig. 6. Spectral specific detectivity (D^*) for 300 K background and f/2 conditions at detector temperatures of 60 K for Sb3019, Sb3020, and Sb3021. The inset shows their 8–12 µm band black-body (BB) D^* as a function of detector temperature for 300 K background and f/2 conditions.

4. NASA Applications

The authors have explored the use of InAs/InAsSb T2SLS detectors for a number of potential NASA applications. One example is the CubeSat Infrared Atmospheric Sounder (CIRAS) [52–54] being developed at the JPL. The CIRAS features a hyperspectral instrument designed to demonstrate MWIR temperature and water vapour sounding on a low-cost space-borne remote-sensing platform. Although InAs/InAsSb MWIR FPAs have already demonstrated excellent imaging performance at 160 K [31, 32], there are special considerations for this hyperspectral instrument where the incident photon flux is dispersed over 625 spectral channels between 4.08 and 5.13 µm. Since the photon flux per pixel in a hyperspectral imager is much lower than for typical imaging applications, much lower dark current density (in this case less than $1 \cdot 10^{-6}$ A/cm^2) is required to achieve the desired sensitivity. However, there is a limit to the amount of cooling that can be provided to the FPA for dark current reduction because of the size-weight-and-power consideration for the CubeSat platform. In the case of CIRAS, it is needed to keep the FPA operating temperature at above 110 K. Therefore, the authors had to pay special attention to suppress detector G-R dark current down to the FPA operating temperature. Figure 7(a) shows an image taken with one of the FPAs developed for the CIRAS project. FPA 17CIL23 is fabricated from wafer Sb3233, with a 3.5 µm thick n-type absorber. At 120 K, devices made from Sb3233 exhibited a 5.4 µm cut-off wavelength, with a dark current density of $1 \cdot 10^{-7}$ A/cm^2. At 115 K, with f/2.2 optics, FPA 17CIL23 demonstrated a mean 3–5 µm band QE of 79.3% with anti-reflection (AR) coating (55.5% without), 18 mK noise equivalent difference temperature (NEDT), and 99.9% operability, and was able to meet the requirements of CIRAS. More discussions are found in Ref. 55.

The authors have also explored LWIR InAs/InAsSb T2SLS infrared detectors for potential NASA land imaging applications. Figure 7(b) shows an image taken with a 10.6 µm cut-off FPA (19PAL02) operating at 68 K. The FPA is fabricated from detector wafer Sb3122, which is a LWIR p-CBIRD sample with a 4.3 µm thick p-type absorber. At 68 operating temperature, the mean FPA dark current density is $3.8 \cdot 10^{-5}$ A/cm^2, and the 8.1–9.5 µm band pass filter QE is 27.5% (without AR coating). The FPA mean NEDT is 29 mK for 300 K background and f/7.7 optics, with an NEDT operability of 99.7%. Results on additional VLWIR detectors and FPAs can be found in Ref. 56.

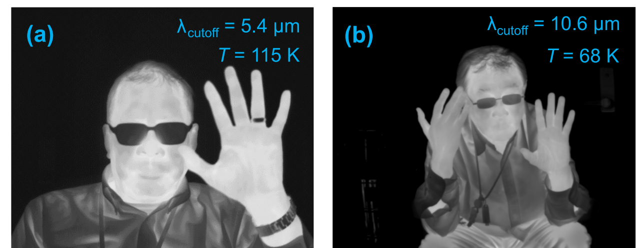

Fig. 7. An image taken from the MWIR FPA 17CIL23 (a), and an image taken from VLWIR FPA 19PAL02 (b). Both are made with InAs/InAsSb T2SLS detector arrays hybridized to the 24 µm pitch, 640×512 format SBF-193 read-out integrated circuit (ROIC).

The Hyperspectral Thermal Emission Spectrometer (HyTES) is a NASA airborne hyperspectral imaging spectrometer with 256 spectral channels between 7.5 and 12 µm [57]. HyTES was first flown in 2012, originally with an LWIR quantum well infrared photodetector (QWIP) FPA. Since 2021, it has been flying with an LWIR InAs/InAsSb T2SLS FPA. Of note is the fact that both the QWIP and the T2SLS FPAs exhibit very good temporal stability and require no in-flight recalibration during observation sessions typically lasting several hours. Yet another LWIR InAs/InAsSb T2SLS FPA is currently being integrated into the Hyperspectral Thermal Imager (HyTI) instrument [58], intended for a low Earth's orbit CubeSat demonstration mission.

5. Conclusions

The InAs/InAsSb T2SLS has emerged as a viable infrared photodetector material in recent years. MWIR InAs/InAsSb T2SLS nBn FPAs exhibit good operating characteristics at 160 K, demonstrating a considerably operating temperature advantage over InSb FPAs. Extending the cut-off wavelength to VLWIR with n-type T2SLS absorber faces challenges in diminishing absorption coefficient and hole mobility that result in a relatively modest QE. One can take advantage of the longer electron diffusion length in p-type absorber for QE enhancement. However, mesa etch exposes p-type InAs/InAsSb T2SLS sidewall surfaces, which invert to degenerate n-type. The

inverted surface is problematic in that (1) it can provide a path for electron surface leakage current, and (2) it leads to the formation of a surface p-n junction that can be a source of dark current. The electron barrier in the CBIRD device architecture can be used to block surface leakage current, but the surface p-n junction problem needs to be addressed with effective passivation. The authors describe some representative results on VLWIR CBIRD devices that contain p-type InAs/InAsSb T2SLS absorbers, and also provide additional references for more in-depth discussion. They also briefly discuss results on InAs/InAsSb T2SLS FPAs for potential NASA applications.

Acknowledgements

The authors wish to thank L. Höglund, E. M. Luong, S. Bandara, J. Mumolo, J. K. Liu, R. E. DeWames, D. R. Rhiger, W. E. Tennant, A. D'Souza, M. A. Kinch, M.B. Reine, J. N. Schulman, M. Tidrow, S. Babu, P. Ghuman, E. Im, J. Hyon, N. Toomarian, and H. Manohara. The research described in this publication was carried out at the Jet Propulsion Laboratory, California Institute of Technology, under a contract with the National Aeronautics and Space Administration (80NM0018D0004).

References

[1] Smith, D. L. & Mailhiot, C. Proposal for strained type II superlattice infrared detectors. *J. Appl. Phys*. **62**, 2545–2548 (1987). https://doi.org/10.1063/1.339468

[2] Osbourn, G. C. InAsSb strained-layer superlattices for long wavelength detector applications. *J. Vac. Sci. Technol. B* **2**, 176 (1984). https://doi.org/10.1116/1.582772

[3] Osbourn, G. C. *et al*. III-V strained layer supperlattices for long-wavelength detector applications: Recent progress. *J. Vac. Sci. Technol. A* **5**, 3150–3152 (1987). https://doi.org/10.1116/1.574857

[4] Tang, P. *et al*. 4–11 pm infrared emission and 300 K light emitting diodes from arsenic-rich $InAs/InAs_{1-x}Sb_x$ strained layer superlattices. *Semicond. Sci. Technol*. **10**, 1177–1180 (1995). https://doi.org/10.1088/0268-1242/10/8/023

[5] Wilk, A. *et al*. Type-II InAsSb/InAs strained quantum-well laser diodes emitting at 3.5 µm. *Appl. Phys. Lett*. **77**, 2298–2300 (2000). https://doi.org/10.1063/1.1317537

[6] Ciesla, C. M. *et al*. Suppression of Auger recombination in arsenic-rich $InAs_{1-x}Sb_x$ strained layer superlattices. *J. Appl. Phys*. **80**, 2994 (1996). https://doi.org/10.1063/1.363157

[7] Lackner, D. *et al*. Strain balanced InAs/InAsSb superlattice structures with optical emission to 10 µm. *Appl. Phys. Lett*. **95**, 081906 (2009). https://doi.org/10.1063/1.3216041

[8] Steenbergen, E. H. *et al*. Significantly improved minority carrier lifetime observed in a long-wavelength infrared III-V type-II superlattice comprised of InAs/InAsSb. *Appl. Phys. Lett*. **99**, 251110 (2011). https://doi.org/10.1063/1.3671398

[9] Connelly, B. C., Metcalfe, G. D., Shen, H. & Wraback, M. Direct minority carrier lifetime measurements and recombination mechanisms in long-wave infrared type II superlattices using time-resolved photoluminescence. *Appl. Phys. Lett*. **97**, 251117 (2010). https://doi.org/10.1063/1.3529458

[10] Donetsky, D., Belenky, G., Svensson, S. & Suchalkin, S. Minority carrier lifetime in type-2 InAs–GaSb strained-layer superlattices and bulk HgCdTe materials. *Appl. Phys. Lett*. **97**, 052108 (2010). https://doi.org/10.1063/1.3476352

[11] Olson, B. V. *et al*. Time-resolved optical measurements of minority carrier recombination in a mid-wave infrared InAsSb alloy and InAs/InAsSb superlattice. *Appl. Phys. Lett*. **101**, 092109 (2012). https://doi.org/10.1063/1.4749842

[12] Höglund, L. *et al*. Influence of radiative and non-radiative recombination on the minority carrier lifetime in midwave infrared InAs/InAsSb superlattices. *Appl. Phys. Lett*. **103**, 221908 (2013). https://doi.org/10.1063/1.4835055

[13] Brown, A. E. *et al*. Characterization of n-type and p-type long-wave InAs/InAsSb superlattices. *J. Electron. Mater*. **46**, 5367–5373 (2017). https://doi.org/10.1007/s11664-017-5621-7

[14] Kim, H. S. *et al*. Long-wave infrared nBn photodetectors based on InAs/InAsSb type-II superlattices. *Appl. Phys. Lett*. **101**, 161114 (2012). https://doi.org/10.1063/1.4760260

[15] Ting, D. Z. *et al*. The emergence of InAs/InAsSb type-II strained layer superlattice barrier infrared detectors. *Proc. SPIE* **11002**, 110020F (2019). https://doi.org/10.1117/12.2521093

[16] Steenbergen, E. H. InAsSb-based Photodetectors. in *Mid-infrared Optoelectronics: Materials, Devices, and Applications* (eds. Tournié, E. & Cerutti, L.) 415–453 (Woodhead Publishing, 2019).

[17] Wu, D., Durlin, Q., Dehzangi, A., Zhang, Y. & Razeghi, M. High quantum efficiency mid-wavelength infrared type-II $InAs/InAs_{1-x}Sb_x$ superlattice photodiodes grown by metal-organic chemical vapor deposition. *Appl. Phys. Lett*. **114**, 011104 (2019). https://doi.org/10.1063/1.5058714

[18] Haddadi, A., Chen, G., Chevallier, R., Hoang, A. M. & Razeghi, M. InAs/ $InAs_{1-x}Sb_x$ type-II superlattices for high performance long wavelength infrared detection. *Appl. Phys. Lett.* **105**, 121104 (2014). https://doi.org/10.1063/1.4896271

[19] Hoang, A. M., Chen, G., Chevallier, R., Haddadi, A. & Razeghi, M. High performance photodiodes based on InAs/InAsSb type-II superlattices for very long wavelength infrared detection. *Appl. Phys. Lett.* **104**, 251105 (2014). https://doi.org/10.1063/1.4884947

[20] Haddadi, A. Chevallier, R., Chen, G. Hoang, A. M. & Razeghi, M. Bias-selectable dual-band mid-/long-wavelength infrared photo-detectors based on $InAs/InAs_{1-x}Sb_x$ type-II superlattices. *Appl. Phys. Lett.* **106**, 011104 (2015). https://doi.org/10.1063/1.4905565

[21] Michalczewski, K. *et al*. Demonstration of HOT LWIR T2SLs InAs/InAsSb photodetectors grown on GaAs substrate. *Infrared Phys. Technol.* **95**, 222–226 (2018). https://doi.org/10.1016/j.infrared.2018.10.024

[22] Delli, E. *et al*. Mid-infrared InAs/InAsSb superlattice nBn photo-detector monolithically integrated onto silicon. *ACS Photonics* **6**, 538–544 (2019). https://doi.org/10.1021/acsphotonics.8b01550

[23] Durlin, Q. *et al*. Midwave infrared barrier detector based on Ga-free InAs/InAsSb type-II superlattice grown by molecular beam epitaxy on Si substrate. *Infrared Phys. Technol.* **96**, 39–43 (2019). https://doi.org/10.1016/j.infrared.2018.10.006

[24] Fastenau, J. M. *et al*. GaSb-based infrared photodetector structures grown on Ge-Si substrates via metamorphic buffers. *SPIE Proc.* **11002**, 110020M (2019). https://doi.org/10.1117/12.2521055

[25] Baril, N. *et al*. Bulk in As_xSb_{1-x} nBn photodetectors with greater than 5 µm cutoff on GaSb. *Appl. Phys. Lett.* **109**, 122104 (2016). https://doi.org/10.1063/1.4963069

[26] Lubyshev, D. *et al*. Effect of substrate orientation on Sb-based MWIR photodetector characteristics. *Infrared Phys. Technol.* **95**, 27–32 (2018). https://doi.org/10.1016/j.infrared.2018.09.031

[27] Lubyshev, D. *et al*. T2SL Mid- and long-wave infrared photodetector structures grown on (211)A, (211)B, and (311)A GaSb substrates. *SPIE Proc*. **11002,** 110020N (2019). https://doi.org/10.1117/12.2521066

[28] Maimon, S. & Wicks, G. W. nBn detector, an infrared detector with reduced dark current and higher operating temperature. *Appl. Phys. Lett*. **89**, 151109 (2006). https://doi.org/10.1063/1.2360235

[29] Ting, D. Z. *et al*. Development of InAs/InAsSb type-II strained layer superlattice unipolar barrier infrared detectors. *J. Electron. Mater.* **48**, 6145–6151 (2019). https://doi.org/10.1007/s11664-019-07255-x

[30] Ting, D. Z., Khoshakhlagh, A., Soibel, A., Hill, C. J. & Gunapala, S. D. Barrier infrared detector, U.S. Patent 8217480 (2012).

[31] Ting, D. Z. *et al*. Mid-wavelength high operating temperature barrier infrared detector and focal plane array. *Appl. Phys. Lett*. **113**, 021101 (2018). https://doi.org/10.1063/1.5033338

[32] Ting, D. Z. *et al*. InAs/InAsSb type-II superlattice mid-wavelength infrared focal plane array with significantly higher operating temperature than InSb. *IEEE Photon, J.* **10**, 1–6 (2018). https://doi.org/10.1109/JPHOT.2018.2877632

[33] Klipstein, P. *et al*. Modeling InAs/GaSb and InAs/InAsSb superlattice infrared detectors. *J. Electron. Mater*. **43**, 2984–2990 (2014). https://doi.org/10.1007/s11664-014-3169-3

[34] Vurgaftman, I. *et al*. Interband absorption strength in long-wave infrared type-II superlattices with small and large superlattice periods compared to bulk materials. *Appl. Phys. Lett*. **108**, 222101 (2016). https://doi.org/10.1063/1.4953035

[35] Ting, D. Z., Soibel, A. & Gunapala, S. D. Hole effective masses and subband splitting in type-II superlattice infrared detectors. *Appl. Phys. Lett*. **108**, 183504 (2016). https://doi.org/10.1063/1.4948387

[36] Ting, D. Z., Soibel, A. & Gunapala, S. D. Type-II superlattice hole effective masses. *Infrared Phys. Technol.* **84**, 102–106 (2017). https://doi.org/10.1016/j.infrared.2016.10.014

[37] Klipstein, P. C. XBn barrier photodetectors for high sensitivity and high operating temperature infrared sensors. *Proc. SPIE* **6940**, 69402U (2008). https://doi.org/10.1117/12.778848

[38] Ting, D. Z., Khoshakhlagh, A., Soibel, A. & Gunapala, S. D. Long wavelength InAs/InAsSb infrared superlattice challenges: a theoretical investigation. *J. Electron. Mater*. **49**, 6936–6945 (2020). https://doi.org/10.1007/s11664-020-08349-7

[39] Ashley, T. & Elliott, C. Nonequilibrium devices for infra-red detection. *Electron. Lett*. **21**, 451–452 (1985). https://doi.org/10.1049/el:19850321

[40] Ashley, T., Elliott, C. & Harker, A. Non-equilibrium modes of operation for infrared detectors. *Infrared Phys*. **26**, 303–315 (1986). https://doi.org/10.1016/0020-0891(86)90008-4

[41] Ashley, T. & Elliott, C. T. Operation and properties of narrow-gap semiconductor devices near room temperature using non-equilibrium techniques. *Semicond. Sci. Technol*. **6**, C99–C105 (1991). https://doi.org/10.1088/0268-1242/6/12c/020

[42] White, A. Generation-recombination processes and Auger suppression in small-bandgap detectors. *J. Cryst. Growth* **86**, 840–848 (1988). https://doi.org/10.1016/0022-0248(90)90813-z

[43] Ting, D. Z.-Y. *et a*l. A high-performance long wavelength superlattice complementary barrier infrared detector. *Appl. Phy. Lett.* **95**, 023508 (2009). https://doi.org/10.1063/1.3177333

[44] Ting, D. Z.-Y. *et al*. Exclusion, extraction, and junction placement effects in the complementary barrier infrared detector. *Appl. Phys. Lett.* **102**, 121109 (2013). https://doi.org/10.1063/1.4798551

[45] Sidor, D. E., Savich, G. R. & Wicks, G. W. Surface conduction in InAs and GaSb. *Proc. SPIE* **9616**, 96160U (2015). https://doi.org/10.1117/12.2188878

[46] Sidor, D. E., Savich, G. R. & Wicks, G. W. Surface leakage mechanisms in III–V infrared barrier detectors. *J. Electron. Mater*. **45**, 4663–4667 (2016). https://doi.org/10.1007/s11664-016-4451-3

[47] Marozas, B. T. *et al*. Surface dark current mechanisms in III-V infrared photodetectors. *Opt. Mater. Express* **8**, 1419 (2018). https://doi.org/10.1364/OME.8.001419

[48] Ting, D. Z., Soibel, A., Khoshakhlagh, A. & Gunapala, S. D. Enhanced quantum efficiency barrier infrared detectors. U. S. Patent No. 10872987 (2020).

[49] Ting, D Z. Long wavelength InAs/InAsSb superlattice barrier infrared detectors with p-type absorber quantum efficiency enhancement. *Appl. Phys. Lett*. **118**, 133503 (2021). https://doi.org/10.1063/5.0047937

[50] Ting, D. Z. *et al*. Long and very long wavelength InAs/InAsSb superlattice complementary barrier infrared detectors. *J. Electron. Mater*. **51**, 4666–4674 (2022). https://doi.org/10.1007/s11664-022-09561-3

[51] Tennant, W. E. "Rule 07" revisited: still a good heuristic predictor of p/n HgCdTe photodiode performance? *J. Electron. Mater*. **39**, 1030–1035 (2010). https://doi.org/10.1007/s11664-010-1084-9

[52] Pagano, T. S., Rider, D., Rud, M., Ting, D. & Yee, K. Measurement approach and design of the CubeSat Infrared Atmospheric Sounder (CIRAS). *Proc. SPIE* **9978**, 997806 (2016). https://doi.org/10.1117/12.2235986

[53] Pagano, T. S. *et al*. CubeSat Infrared Atmospheric Sounder technology development status. *J. Appl. Remote Sens.* **13**, 032512 (2019). https://doi.org/10.1117/1.JRS.13.032512

[54] Pagano, T. S., Schwochert, M. & Rafol, S. Ambient performance testing of the CubeSat Infrared Atmospheric Sounder (CIRAS). *Proc. SPIE* **11832**, 118320D (2021). https://doi.org/10.1117/12.2593625

[55] Ting, D. Z. *et a*l. Type-II superlattice mid-wavelength infrared focal plane arrays for CubeSat Hyperspectral Imaging. *IEEE Photon. Technol. Lett.* **34**, 329–332 (2022). https://doi.org/10.1109/LPT.2022.3156048

[56] Ting, D. Z. *et al*. Development of type-II superlattice long wavelength infrared focal plane arrays for land imaging. *Infrared Phys. Technol.* **123**, 104133 (2022). https://doi.org/10.1016/j.infrared.2022.104133

[57] Hyperspectral Thermal Emission Spectrometer website. *NASA/Jet Propulsion Laborator*y, *California Institute of Technology* https://hytes.jpl.nasa.gov (2023).

[58] Wright, R. *et al*. HYTI: thermal hyperspectral imaging from a CubeSat platform. *Proc. SPIE* **11131**, 111310G (2019). https://doi.org/10.1117/12.2530821